Single Crystalline $Ge_{1-x}Mn_x$ Nanowires as Building Blocks for Nanoelectronics

Machteld I. van der Meulen[†,ϕ], Nikolay Petkov[†,ϕ], Michael A. Morris[†,ϕ], Olga Kazakova[‡], Xinhai Han[#], Kang L. Wang[#], Ajey P. Jacobs[§] and Justin D. Holmes[,†,ϕ]*

Materials and Supercritical Fluids Group, Department of Chemistry and the Tyndall National Institute, University College Cork, Cork, Ireland. Centre for Research on Adaptive Nanostructures and Nanodevices (CRANN), Trinity College Dublin, Dublin 2, Ireland. National Physical Laboratory, Teddington, UK. Department of Electrical Engineering, University of California, Los Angeles, CA, USA. § TMG External Programs, Intel Corporation, Santa Clara, California 95052, USA

[*]Corresponding author, j.holmes@ucc.ie, tel. +353 21 4903608, fax +353 21 4274097

RECEIVED DATE (to be automatically inserted after your manuscript is accepted if required according to the journal that you are submitting your paper to)

[†] Materials and Supercritical Fluids Group, Department of Chemistry and the Tyndall National Institute, University College Cork, Ireland.

[ϕ] Centre for Research on Adaptive Nanostructures and Nanodevices (CRANN), Trinity College Dublin, Dublin 2, Ireland

[‡] National Physical Laboratory, Teddington, UK

Department of Electrical Engineering, University of California, Los Angeles, CA, USA

[§] TMG External Programs, Intel Corporation, Santa Clara, California 95052, USA

Magnetically doped Si and Ge nanowires have potential application in future nanowire spin-based devices. Here, we report a supercritical fluid method for producing single crystalline Mn-doped Ge nanowires, with a Mn-doping concentration of between 0.5-1.0 atomic %, that display ferromagnetism above 300 K and a superior performance with respect to the hole mobility, of around 340 cm^2/Vs, demonstrating the potential of using these nanowires as building blocks for electronic devices.

Group-IV semiconductor nanowires are of particular interest for integration into future nanoscale device structures, as they are compatible with existing complementary metal-oxide-semiconductor (CMOS) technologies. Single crystalline Ge and Si nanowires[1,2] have recently been synthesized, isolated and utilized in various charge-based nanowire devices, such as field-effect transistors, integrated logic gates, memory devices, nanolasers and photodetectors[3,4]. However, operational nanowire spin-state devices such as spin gain transistors and spin injection devices have not yet been demonstrated. Theoretical predictions show that such devices can be realized by employing dilute magnetic semiconductors (DMS)[5], as these materials combine the complementary functionalities of ferromagnetic and semiconductor materials[6-8].

After predicting[9,10] and reporting ferromagnetism in Mn-doped germanium for the first time[11] many papers have been published on $Ge_{1-x}Mn_x$ DMS materials. Most research has focused on nanocrystals[12] and thin-films[13-20] prepared via ion implantation and molecular beam epitaxy (MBE). In these materials, a Curie temperature (T_c) of 296 K is usually attributed to the formation of the intermetallic precipitate Mn_5Ge_3, while diluted Mn atoms in the Ge matrix result in a T_c of 115 K and ferromagnetic remanence below 20 K[11,21]. Superparamagnetic and ferromagnetic behavior is observed when manganese-rich nanostructures are formed within the Ge matrix[22,23].

Recently the synthesis of single crystalline $Ge_{1-x}Mn_x$ nanowires via a thermal vapor transport method was reported[24-26]. The authors claim the incorporation of 8 %[24,25], and even up to 20 %, Mn^{2+} ions[26] in the Ge matrix, without observing substantial disorder of the single crystalline Ge lattice, even though the limited solubility of transition metals in a semiconductor matrix usually leads to phase separation or spinodal decomposition. However, these wires possessed a thick oxide shell possibly containing amorphous MnO.

In this work, the supercritical fluid-liquid-solid (SFLS) method developed for producing single crystalline Ge and Si nanowires[2,27-29], was adapted to grow single crystalline $Ge_{1-x}Mn_x$ nanowires. We report on the structural properties of these nanowires and demonstrate they are promising building blocks for both electronic and potentially spintronic devices.

Freestanding nanowires were synthesized by a SFLS method using sputtered gold nanoparticles, supported on porous alumina membranes (Whatman, nominal pore diameter 100 nm), as catalytic seeds for growth. The reaction was performed as an injection flow-through reaction, in which the porous support was placed inside a reactor cell and the precursor mixture containing 10 ml of anhydrous hexane, 0.1 ml of diphenylgermane, as the germanium precursor, and 0.005 g of dimanganese dodecacarbonyl as a manganese precursor was loaded into a premixing cell. Loading and sealing of the reaction and premixing cell were carried out under a nitrogen atmosphere in a glove box. The reaction cell and premixing cell were attached to a high-pressure CO_2 pump. The temperature and pressure of the reaction cell were raised to 723 K and 6.9 MPa respectively. The pressure in the premixing cell was raised to 20.7 MPa and the precursor solution was injected into the reaction cell at a flow rate of 1.0-1.5 mL min^{-1} for 45 min. After the reaction, the cell was cooled to room temperature and depressurized.

A top view SEM image of freestanding Ge_xMn_{1-x} nanowires as prepared is shown as an inset in Figure 1b. The diameters of the wires range between 30-100 nm. In the XRD pattern obtained from the nanowires (Figure 1a) reflections at 2θ values of 27.4, 45.6 and 53.8° were observed, corresponding to

the {111}, {220}, and {331} set of planes for a diamond cubic germanium lattice (JCPDS card no. 04-0545). The reflection at a 2θ value of 38.5 corresponds to the Au-Ge alloy that is formed at the interface of the Ge nanowires with the catalytic gold seed. The XRD pattern showed no evidence for the presence of secondary phase ferromagnetic alloys, such as for example the Mn_5Ge_3 phase. However, it is unlikely that a dilute secondary phase at the nanoscale can be detected by conventional XRD. A large number of Ge_xMn_{1-x} nanowires were analyzed via Energy Dispersive X-ray (EDX) spectroscopy. Figure 1a shows a typical EDX spectrum (as inset) of a Ge_xMn_{1-x} nanowire clearly showing the Mn K_α peak. EDX analysis revealed an average Mn concentration of 0.5-1.0 atomic %. The nanowires were further analyzed by HRTEM imaging. A typical HRTEM image of a Ge_xMn_{1-x} nanowire is shown in Figure 1c. The nanowire shows a perfect crystal structure, with the observed lattice planes corresponding to the [111] plane of the Ge lattice with a d-spacing of 3.3 Å. Electron Diffraction of the HRTEM image (inset) shows that the nanowire was viewed along the [111] zone axis and confirms that the Ge_xMn_{1-x} nanowires are single-crystalline and exhibit the cubic diamond structure. Secondary phases, nanoscale precipitates or large lattice distortions in the Ge lattice were not detected. Remarkably, no oxide shell was observed on the surface of many of the Mn-doped Ge nanowire directly after their synthesis. Additionally, elemental Mn maps of individual nanowires were obtained by Electron Energy Loss Spectroscopy (EELS) mapping (Figure 1d-f). The Mn maps confirm the presence of Mn in the nanowires. HRTEM imaging excluded the formation of secondary phases, but the formation of Mn-rich and Mn-depleted regions cannot be completely ruled out. However, Mn rich nanoclusters with concentrations up to 15 %, such as observed by Bougeard et al.[30] and Ge_2Mn nanocolumns observed by Jamet et al.[22] in thin films, were not detected.

Extended X-ray absorption fine structure (EXAFS) were undertaken to further investigate the structural properties of the $Ge_{1-x}Mn_x$ nanowires. Figure 2a shows the Ge K-edge EXAFS spectrum of the $Ge_{1-x}Mn_x$ nanowires. The best fit results of the Ge K-edge, with an excellent R value of 15, are summarized in Table 1. Ge is surrounded by three shells of Ge atoms at distances of 2.45, 4.01 and 4.71 Å, which

confirms the perfect single crystalline nature of the Ge lattice. The calculated bond distances do not show any expansion of the Ge lattice, which suggests that Mn atoms are substitutionally diluted in the Ge host lattice. This is in agreement with electronic structure calculations which show that Mn impurities preferentially occupy the substitutional site[11]. Furthermore, an isolated substitutional Mn creates only negligible distortion of the host lattice, with neighboring Ge atoms perturbed by less than 0.05 Å. Also the EXAFS data at the Ge K-edge did not show a Ge-O bonding peak in agreement with earlier observations that an oxide shell is absent. The Mn K-edge EXAFS spectrum is shown in Figure 2b and the best fit results are summarized in Table 2. Mn EXAFS data were collected in fluorescence mode and are as a result noisier than the Ge EXAFS data. The R value of 36 is therefore a good fit. At the Mn K-edge the first shell is observed at 2.11 Å, which is typical for a Mn-O bond. EXAFS is a bulk technique and therefore the whole sample is analyzed, including a by-product that was obtained during SCF growth in the form of a particulate material (seen by SEM). This allows us to attribute the Mn-O bond to the by-product. Most importantly, the next-nearest neighbor for Mn is Ge at a bond distance of 2.40. *Ab initio* electronic structure calculations by Continenza et al. show that when a Mn impurity is incorporated into a single crystalline Ge-matrix, the Mn-Ge distance is 2.38 for Mn at a substitutional site and 2.48 Å for Mn at an interstitial site respectively[31]. Our EXAFS data therefore implies that the Mn atoms are incorporated into the Ge lattice at substitutional sites.

For magnetization measurements nanowires were harvested from an AAO template and measured in a powder form. Figure 3a demonstrates the field dependence of the magnetic moment for single crystalline $Ge_{1-x}Mn_x$ nanowires. The M vs. B dependencies were measured at temperatures between 5 and 300 K. After background subtraction the curves show saturation at $B \approx 0.3$ T (Figure 3a and d). All M vs. B dependencies demonstrate a week hysteretic behavior over the whole temperature range. The hysteresis is characterized by a small coercive field (B_c = 82 Oe and 154 Oe at T = 300 K and 5 K, respectively, Figure 3c) and remanence, M_R/M_S = 0.10-0.16. Both the remanence and saturation are weakly temperature dependent (Figure 3d). A well-defined saturation of the magnetic moment, presence

of a finite (although rather small) coercive field and remanence at room temperature are typical for a weak ferromagnet.

The temperature dependences of magnetization have been measured during field cooling (FC) and zero-field cooling (ZFC) procedures at B = 100 mT (Figure 3b). Overall, the low-temperature increase of magnetization is relatively small, about 20 % above its room-temperature value for the FC curve. The figure clearly demonstrates two transition temperatures T_{C1} = 16 K and T_{C2} = 63 K. In the low temperature regime ($T<T_{C1}$), the magnetization sharply drops as the temperature increases signifying the presence of the paramagnetic component of the magnetization. The 2nd critical temperature indicates the most pronounced phase transition. As performed magnetic measurements are related to the whole sample, the measured transition temperature T_{C2} could, be attributed to an external oxygen-containing phase as structural characterization shows that Mn is partially oxidized as a by-product of the synthesis. Mn_3O_4[32], a ferromagnetic manganese oxide, exhibits a phase transition in bulk at somewhat lower temperature, T_C (Mn_3O_4) = 42 K. The magnetic properties of Mn_3O_4 nanocrystals were also widely investigated and their Curie temperature was shown to be weakly temperature dependent[33-38]. In the majority of studies, the T_C of Mn_3O_4 nanoparticles is smaller than the corresponding bulk value and drops as the particle size decreases. For example, transition temperatures of 40.9, 39.0 and 37.8 K were measured for samples with particle sizes of 13.4, 9.7 and 5.0 nm, respectively[36]. The opposite trend was observed in a work by Chang et al, where the Curie temperature of nanoparticles exceeded the bulk value and reached the maximum of 44.3 K. However, in all these cases the transition temperature is significantly smaller than T_{C2}=63 K measured in the present study. Moreover, a very high coercive field, up to 7.5 kOe, was reported in all work cited above. Antiferromagnetic manganese monoxide, MnO, exhibits a Neel temperature, T_N, of 122 K in its bulk state[39] and the blocking temperature (T_B) of MnO nanoparticles is about 19-30 K[38,39] which is also significantly lower than the T_B experimentally observed here. Additionally, MnO nanoparticles are also characterized by a large coercive field (e.g. up to 1.75 kOe[38]). Antiferromagnetic MnO_2 exhibits a Neel transition at 86 K[39]which also does not

correspond to our experimental results. Thus, the obtained by-product is probably a more complex compound containing carbon and oxygen, than one of these 'standard' manganese oxides. However we can rule out that these compounds can be responsible for the observed room-temperature ferromagnetism as discussed below.

At $T>T_{C2}$ the *m(B)* dependence is characterized by a small hysteretic effect and a well-pronounced magnetization saturation and hence, can be attributed to ferromagnetic interactions between diluted Mn ions. As the averaged resulting concentration of Mn defects is relatively low (x = 0.5-1 atomic%), the observed ferromagnetism is weak, but the critical temperature of the ferromagnetism exceeds 300 K. The exact T_c was not directly measured in our experiments and high temperature measurements are necessary for determination. The origin of the high-temperature ferromagnetism in $Ge_{1-x}Mn_x$ nanowires with low averaged concentration of Mn is unknown at this stage. The existence of typical binary GeMn alloys (such as Mn_5Ge_3, $Mn_{11}Ge_8$) was clearly ruled out. In general, spinodal decomposition (alternating regions with low and high concentrations of magnetic ions) is considered to be the source of the high-temperature ferromagnetism[40] and has been observed in many DMS systems including GeMn semiconductors[22,30] The weak room-temperature ferromagnetism observed in our $Ge_{1-x}Mn_x$ nanowires could originate from areas rich in diluted Mn atoms, while areas low in Mn concentration could be responsible for the low-temperature paramagnetic signal. This would be in good correspondence with the trends described above as some kind of structural decomposition and inhomogeneous distribution of Mn in the Ge host could not completely be ruled out.

With an electronic configuration of $3d^5 4s^2$, a magnetic moment of 5 μ_B is expected for Mn at a substitutional site in a Ge lattice. But electronic structure calculations show a reduced magnetic moment of about 3 μ_B per Mn atom due to strong hybridization between *d* states of Mn and *p* states of Ge[11,31]. The maximum measured saturation moment per Mn atom in our samples was calculated to be around 0.8 μ_B at T = 5 K and drops to 0.7 μ_B at T = 300 K. However, it must be stated this is a rough

estimation as there might be some experimental error in determining the mass of the powdered nanowire samples measured by SQUID, due to the small quantities of samples produced. Further, spinodal decomposition could have an influence on the reduced magnetic moment. In areas with lower concentration Mn does not contribute to the magnetic moment. But in areas with higher concentrations of Mn the effective moment will be higher than averaged. However, determining the magnetic moment requires further investigation.

To produce a single $Ge_{1-x}Mn_x$ nanowire field effect transistor device, drops of a $Ge_{1-x}Mn_x$ suspension in isopropyl alcohol (IPA) were pipetted onto a degenerative doped Si wafer coated with 300 nm thermal oxide, which had prefabricated Ti/Au probe pads patterned by optical lithography. Electron Beam Lithography (EBL) was used to define the contacts between the nanowires and the probe pads. Before metal deposition, the nanowires were dipped in diluted HF (10 %) for 2~3 seconds to remove native oxide in the contact regions. 180 nmTi/ 20nm Au were deposited using electron beam evaporation as source and drain contacts. Electrical measurements were performed using a home-built probe station connected to a Keithley 4200 semiconductor parameter analyzer. A SEM image of the FET (inset of Figure 4a) shows a 1.4 μm long $Ge_{1-x}Mn_x$ nanowire contacted by the source and drain electrodes. The electrical properties of our $Ge_{1-x}Mn_x$ nanowire FETs exhibit p-type depletion mode behavior. Although intrinsic germanium displays a p-type depletion mode behavior as well, it has been found that this is the result of accumulated holes at the semiconductor surface. While the surface states do induce hysteresis their highest density in Ge has been found to be less than $10^{15}/cm^2$ [41]. Also, there are reports that CVD grown intrinsic Ge nanowire devices are unintentionally p-doped from the growth system[42]. Therefore, our results can be attributed to the acceptor levels introduced by Mn atoms in germanium[43] which provide a carrier concentration of $10^{16}/cm^3$. An on/off current ratio (I_{on}/I_{off}) of ~ 10^4 at -0.1 V source-drain bias (V_{ds}) and a subthreshold swing (SS) of 210 mV/decade (Figure 4b) were obtained. The maximum transconductance (g_m) at V_{ds}=-0.1 V is 0.2 μS. A small hysteresis in the transfer characteristics is found during a dual sweep which is very common for Ge nanowire FETs and possibly

caused by surface oxide species[44,45]. Note that even though the $Ge_{1-x}Mn_x$ nanowires were dipped into HF prior to the S/D metal deposition, only the oxides under the S/D region were removed, but the oxides in the channel region were not removed. Surface passivation might help to minimize the hysteresis[42]. I_{ds}-V_{ds} curves at various V_{gs} (Figure 4b) show an on-current of 2.2 μA at V_{ds}= -0.5 V.

The field effect hole mobility μ can be estimated from the transconductance (g_m) at a fixed S/D bias (V_{ds}) by using equation (1)

$$\mu = \frac{g_m L^2}{V_{ds} C_{ox}} \qquad (1)$$

where L is the channel length (~ 1.4 μm) and C_{ox} is the coupling capacitance between the $Ge_{1-x}Mn_x$ nanowire channel and the back-gate SiO_2. C_{ox} can be calculated using the cylinder-on-plate model[46]

$$C_{ox} = \frac{2\pi\varepsilon_0\varepsilon L}{\cosh^{-1}(\frac{r + t_{ox}}{r})} \qquad (2)$$

where $\varepsilon_0 = 8.85\times10^{-12} F/m$ is vacuum permittivity, ε ~3.9 is the dielectric constant, r =50 nm is the radius of the $Ge_{1-x}Mn_x$ nanowire, and t_{ox} =300 nm is the thickness of gate oxide. The estimated capacitance is then $C_{ox} \sim 1.15\times10^{-16} F$, from which a mobility of ~ 340 cm^2/Vs is obtained. The Mn doped Ge devices show superior performance with respect to the mobility of intrinsic Ge nanowire FET devices. For example, the mobility for SFLS grown Ge nanowires was found to be less than 10 cm^2/Vs for various post growth processing of the as grown nanowires[45]. Additionally, Ge nanowires grown by CVD in the absence of B_2H_2 have been found to be highly insulating[47]. The mobility of our $Ge_{1-x}Mn_x$ nanowire FET is lower than the highest reported mobility of 730 cm^2/Vs for Si/Ge heterostructured nanowire FETs[48] and that of 600 cm^2/Vs reported for boron-doped single crystalline nanowires [47]. However, in these FETs the strain induced Si layer accounted for the superior performance and surface passivation respectively. When the capacitance was calculated using the cylinder-on-plate model, we assumed our nanowires are completely embedded in the dielectric material. However, in our back gated

FET, the nanowires are not embedded in the dielectric materials, so the calculated capacitance is in the upper limit using this model. This can be accounted for by an effective dielectric constant of 2.2 for SiO_2 within the analytical model of the embedded nanowires[49]. Therefore, the mobility could be ~ 600 cm^2/Vs, which is comparable to the highest value of Ge nanowire FETs. The carrier concentration (n_e) can be calculated using equation (3)

$$n_e = \frac{V_{th} C_{ox}}{q \pi r^2 L} \qquad (3)$$

where q is elementary charge and the threshold voltage (Vth) ~ 0.53 V (extracted from the transfer characteristics). The carrier density is estimated to be ~ $3.5\times10^{16}/cm^3$. It should be noted that the carrier concentration could be overestimated due to overestimated C_{ox}. If the effective dielectric constant (2.2) of SiO_2 is used to calculate the C_{ox} instead of 3.9, the carrier concentration is ~ $2.0\times10^{16}/cm^3$.

In conclusion, we have synthesized single-crystalline $Ge_{1-x}Mn_x$ nanowires with an average Mn concentration of 0.5-1.0 %. EXAFS data show that the Mn atoms occupy substitutional sites. The formation of secondary phases was excluded by HRTEM. However, we observed the coexistance of a few magnetic sublattices in the single crystalline nanowires. The room-temperature ferromagnetism most likely originates from areas rich in diluted Mn ions, while areas with depleted Mn concentration (< 0.5 atomic%) are magnetically non-active. Increasing of the resulting Mn concentration could enhance ferromagnetism in the single crystalline nanowires. Alternatively, co-doping with a non-magnetic impurity (such as As[50]) can also raise the carrier concentration and facilitate ferromagnetism. A back-gated FET based on these single-crystalline nanowires shows an on/off ratio of nearly 10^4, threshold voltage of ~0.53 V, maximum transconductance of 0.2 μS and a subthreshold swing of 210 mV/decade. The mobility was estimated around 340 cm^2/Vs demonstrating that these nanowires are promising building blocks for both electronic and spintronic devices.

The authors acknowledge the financial support from the Irish Research Council for Science, Engineering and Technology (IRCSET). The authors also acknowledge the European Synchrotron Radiation Facility (ESRF) for the use the DUBBLE-CRG beamline (BM 26a) and GILDA-CRG beamline (BM08). Further we acknowledge Oxford University and the European Community in arising from ESTEEM visit (contract no. 026019). This work was partially funded under the UK DIUS's NMS project ESQ01T1.

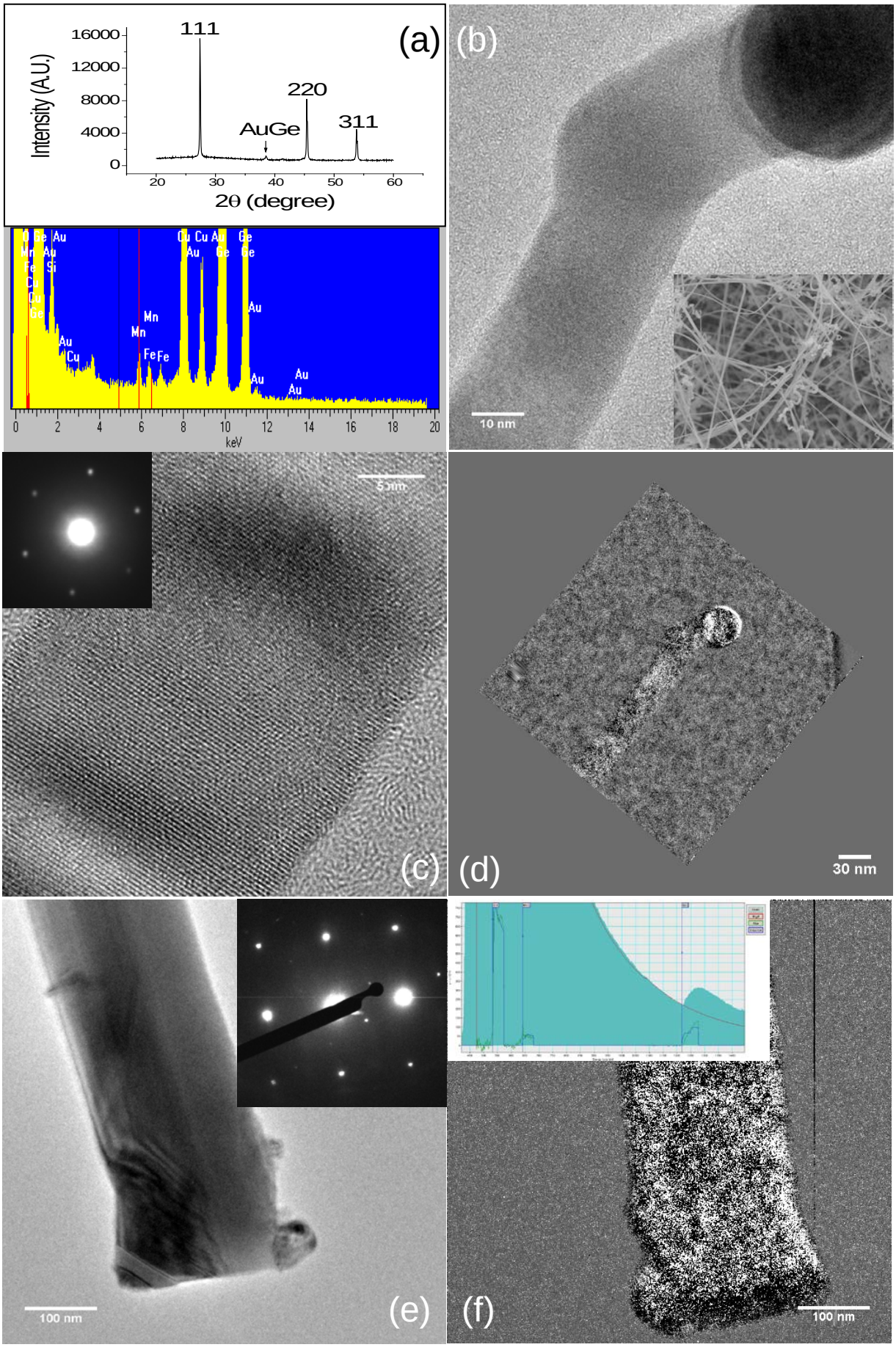
(a)
Intensity (A.U.)
16000
12000
8000
4000
0
111
220
AuGe
311
20
30
40
50
60
2θ (degree)
(b)
10 nm
Au
Cu
Ge
Mn
Fe
Si
keV
0
2
4
6
8
10
12
14
16
18
20
5 nm
(c)
(d)
30 nm
(e)
100 nm
(f)
100 nm

Figure 1 (a) XRD pattern of Ge_xMn_{1-x} NWs showing the (111), (220) and (331) planes of the diamond cubic Ge lattice and Au-Ge alloy formed with catalytic seed and EDX spectrum of a single Ge_xMn_{1-x} NW clearly showing Mn peak (Fe peaks are inherent to detector) (b) TEM image of a 30 nm Ge_xMn_{1-x} NW. The inset is showing SEM image of Ge_xMn_{1-x}. (c) HRTEM image of a 30 nm Ge_xMn_{1-x} NW showing the Ge (111) lattice with a d-spacing of 3.3 Å. The inset is showing the Electron Diffraction pattern of the NW (d) Mn map of a 30 nm Ge_xMn_{1-x} NW (same as in Fig. 1b) obtained by EELS mapping. (e) TEM image of a 180 nm Ge_xMn_{1-x} NW. The inset is showing the Electron Diffraction pattern of the NW. (f) Mn map of a 180 nm Ge_xMn_{1-x} NW (same as in Fig. 1e) obtained by EELS mapping. The inset is showing the EELS spectrum clearly revealing the presence of the Mn peak at L-edge.

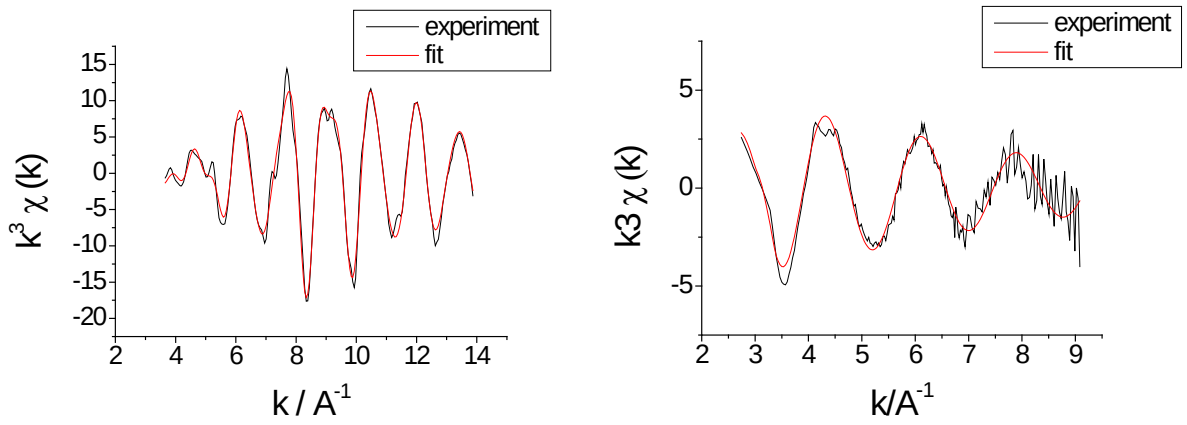

Figure 2 EXAFS of Ge_xMn_{1-x} NWs showing the obtained spectrum and best fit at (a) Ge K-edge and (b) Mn K-edge.

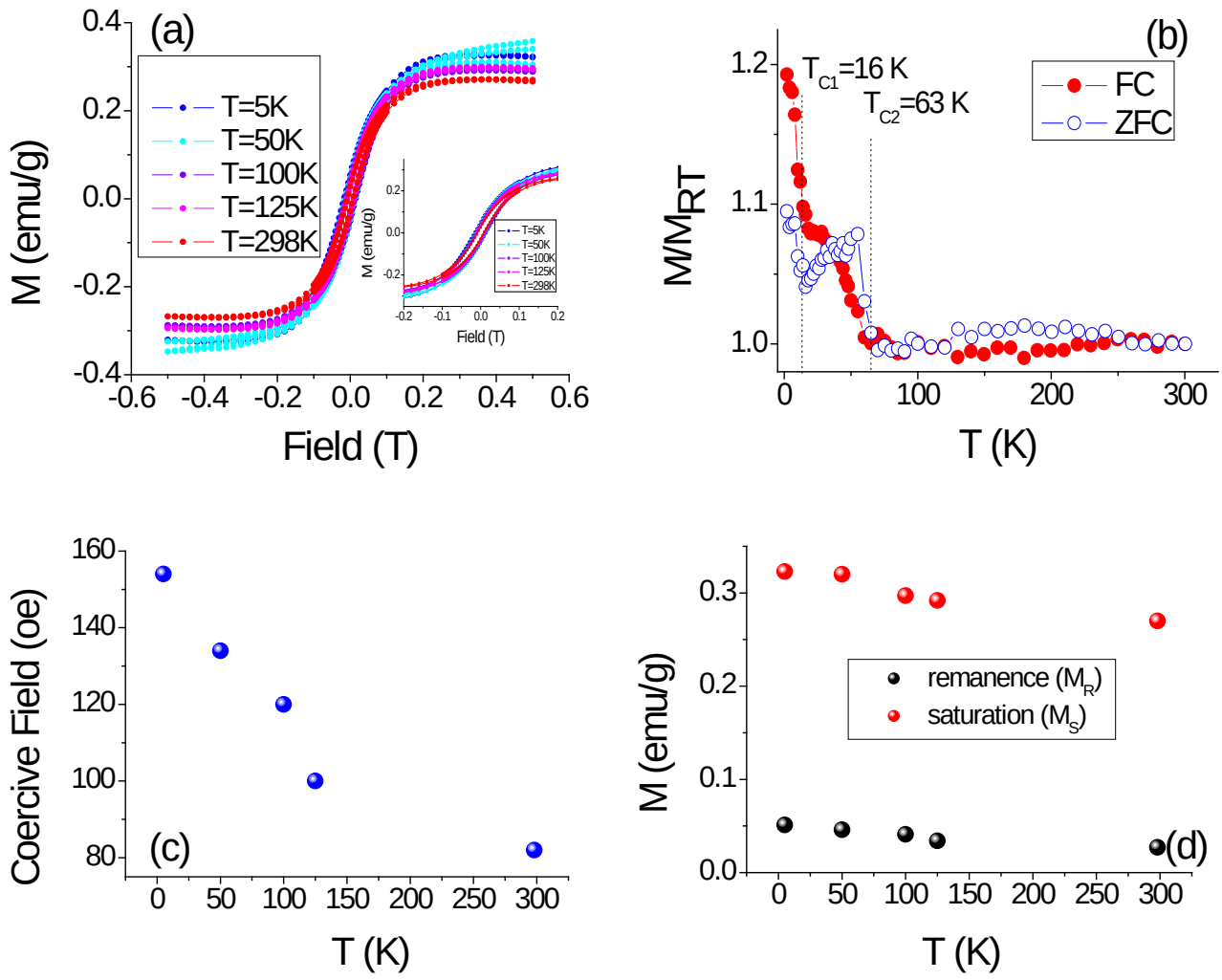

Figure 3 (a) Field dependencies of the magnetization in $Ge_{1-x}Mn_x$ nanowires. Inset shows the *m(B)* dependencies in low magnetic field (b) Temperature dependencies of the magnetization (*B*= 100 mT) normalized to its room temperature value (c) Coercivity at temperatures 5-300 K and (d) Saturation & Remanence at temperatures 5-300 K.

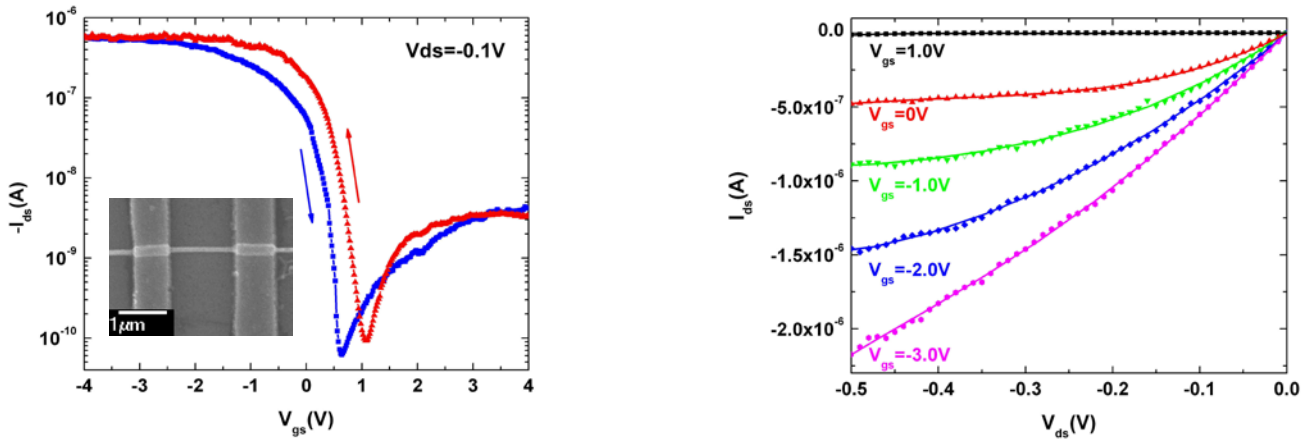

Figure 4 (a) Transfer I_{ds}-V_{gs} and (b) output characteristics I_{ds}-V_{ds} at various gate bias of a single Mn_xGe_{1-x} nanowire Field Effect Transistor. Inset of (a): SEM image of the FET.

Table 1 EXAFS fitting results of $Ge_{1-x}Mn_x$ NWs at Ge K-edge exhibiting a best of fit parameter of R = 15

Shell	Atom	Distance (Å)
T1	Ge	2.45
T2	Ge	4.01
T3	Ge	4.71

Table 2 EXAFS fitting results of $Ge_{1-x}Mn_x$ NWs at Mn K-edge exhibiting a best of fit parameter of R = 36.

Shell	Atom	Distance (Å)
T1	O	2.11
T2	Ge	2.40

References

(1) Hanrath, T.; Korgel, B. A.; *J. Am. Chem. Soc*, **2002**, *124*, 1424-1429

(2) Holmes, J. D.;Johnston, K. P.; Doty, R. C.; Korgel, B. A.; *Science*, **2000**, *287*, 1471-1473

(3) Lieber, C. M.; Wang, Z. L., *MRS Bulletin*, **2007**, *32*, 99-108

(4) Hang, Y.; Duan, X.; Wei, Q. ; Lieber, C. M.; *Science*, **2001**, *291*, 630-633

(5) Ohno, H.; Chiba, D.; Matsukura, F.; Omiya, T.; Abe, E.; Dietl, T.; Ohno, Y.; Ohtani, K.; *Nature*, **2000**, *408*, 944-946

(6) Ohno, H.; *Science*, **1998**, *281*, 951-956

(7) Dietl, T.; *Los Alamos National Laboratory, Preprint Archive, Condensed Matter*, **2002**, 1-8

(8) Dietl, T.; *Nature Materials*, **2003**, *2*, 646-648

(9) Dietl, T.; Ohno, H.; Matsukura, F,; Cibert, J.; Ferrand, D.; *Science*, **2000**, *287*, 1019-1022

(10) Dietl, T.; Ohno, H.; Matsukura, F.; *Phys. Rev. B: Condensed Matter and Material Physics*, **2001**, *63*, 195205/1-195205/21

(11) Park. Y. D.; Hanbicki, A. T.; Erwin, S. C.; Hellberg,,C. S.; Sullivan, J. M.; Mattson, J. E.; Ambrose, T. F.; Wilson, A.; Spanos, G.; Jonker, B. T.; *Science*, **2002**, *295*, 651-654

(12) Kang, J.-S.; Kim, G.; Wi, S. C.; Lee, S. S.; Choi, S.; Cho, S.; Han, S. W.; Kom, K. H.; Song, H. J.; Shin, H. J.; Sekiyama, A.; Kasai, S.; Suga, S.; Min, B. I.; *Phys. Rev. Lett.*, **2005**, *94*, 147202/1-147202/4

(13) Passacantando, M.; Ottaviano, L.; D'Orazio, F.; Lucari, F.; De Biase, M.; Impellizzeri, G.; Prioli, F.; *Phys. Rev. B: Condensed Matter and Material Physics*, **2006**, *73*, 195207/1-195207/5

(14) Pinto, N.; Morresi, L.; Ficcadenti, M.; Murri, R.; D'Orazio, F.; Lucari, F.; Boarino, L.; Amato, G.; *Phys. Rev. B: Condensed Matter and Material Physics*, **2005**, *72*, 165203/1-165203/7

(15) Zeng, C.; Zhu, w.; Erwin, S. C.; Zhang, Z.; Weitering, H. H.; *Phys. Rev. B: Condensed Matter and Material Physics*, **2004**, *70*, 205340/1-205340/8

(16) Li, A. P.; Wendelken, J. F.; Shen, J.; Feldman, L. C.; Thompson, J. R.; Weitering, H. H.; *Phys. Rev. B: Condensed Matter and Material Physics*, **2005**, *72*, 195205/1-195205/9

(17) Ahlers, S.; Bougeard, D.; Sircar, N.; Abstreiter, G.; Trampert, A.; Opel, M.; Gross, R.; *Phys. Rev. B: Condensed Matter and Material Physics*, **2006**, *74*, 214411/1-214411/8

(18) Bihler, C.; Jaeger, C.; Vallaitis, T.; Gjukic, M.; Brandt, M. S.; Pippel, E.; Woltersdorf, J.; Gosele, U.; *Appl. Phys. Lett.*, **2006**, *88*, 112506/1-112506/3

(19) Chen, J.; Wang, K. L.; Galatsis, K. *Appl. Phys. Lett.*, **2007**, *90*, 012501/1-012501/3

(20) Padova, P. D.; Ayoub, J.-P.; Berbezier, I.; Perfetti, P.; Quaresima, C.; Testa, A. M.; Fiorani, D.; Olivieri, B.; Mariot, J.-M.; Taleb-Ibrahimi, A.; Richter, M. C.; Heckmann, O.; Hricovini, K.; *Phys. Rev. B: Condensed Matter and Material Physics*, **2008**, *77*, 045203/1-045203/7

(21) Li, A. P.; Shen, J.; Thompson, J. R.; Weitering, H. H.; *Appl. Phys. Lett*, **2005**, *86*, 152507/1-152507/3

(22) Jamet, M.; Barski, A.; Devillers, T.; Poydenot, V.; Dujardin, R.; Bayle-Guillemaud, P.; Rothman, J.; Bellet-Amalric, E.; Marty, A.; Cibert, J.; Mattana, R.; Tatarenko, S.; *Nature Materials*, **2006**, *5*, 653-659

(23) Deviller, T.; Jamet, M.; Barski, A.; Poydenot, V.; Bayle-Guillemaoud, P.; Bellet-Amalric, E.; *Phys. Rev. B.*, **2007**, *76*, 205306/1-205306/12

(24) Grossi, V.; Bussolotti, F.; Passacantando, M.; Santucci, S.; Ottaviano, L.; *Superlattices and Microstructures*, **2008**, doi:10.1016/j.spmi,2007.12.007

(25) Grossi, V.; Parisse, P.; Passacantando, M.; Santucci, S.; Impellizzeri, G.; Irrera, A.; Ottaviano, L.; *Appl. Surf. Sci.*, **2008**, *254*, 8093-8097

(26) Cho, Y. J.; Kim, C. H.; Kim, H. S.; Lee, W. S.; Park S.-H.; Park, J.; *Chem. Mater.*, **2008**, *20*, 4694-4702

(27) Tuan, H.-Y.; Lee, D. C.; Hanrath, T.; Korgel, B. A.; *Chem. Mater.*, **2005**, *17*, 5705-5711

(28) Hanrath, T.; Korgel, B. A.; *Advanced Materials*, **2003**, *15*, 437-440

(29) Petkov, N.; Birjukkovs, P.; Phelan, R.; Morris, M. A.; Erts, D.; Holmes, J. D.; *Chem. Mater.*, **2008**, *20*, 1902-1908

(30) Bougeard, D.; Ahlers, S.; Trampert, A.; Sircar, N.; Abstreiter, G.; *Phys. Rev. Lett.* **2006**, *97*, 237

(31) Continenza, A.; Profeta, G.; Piccozi, S.; *Phys. Rev. B: Condensed Matter and Material Physics*, **2006**, *73*, 035212/1-035212/10

(32) Hauback, B. C.; Helmer, F.; Sakai, N.; *J. Solid State Chem.* **1996**, *124*, 43

(33) Yang, L.-X.; Zhu, Y.-J., Tong, H.; Wang, W.-W.; Cheng, G.-F.; *J. Solid State Chem.*, **2006**, *179*, 1225-1229

(34) Lei, S.; Tang, K.; Fang, Z.; Sheng, J.; *J. Of Nanoparticle Research*, **2007**, *9*, 833-840

(35) Wang, N.; Guo, L.; He, L.; Cao, X.; Chen, C.; Wang, R.; Yang, S.; *Small*, **2007**, *3*, 606-610

(36) Zhao, N.; Nie, W.; Liu, X.; Tian, S.; Zhang, Y.; Ji, X.; *Small*, **2008**, *4*, 77-81

(37) Ghosh, M.; Biswas, K.; Sundaresan, A.; Rao, C. N. R.; *Journal of Mat. Chem.*, **2006**, *16*, 106-111

(38) Djerdj, I.; Arčon, D.; Jagličić, Z.; Niederberger, M.; *J. Phys. Chem. C.*; **2007**, *111*, 3614-3623

(39) Morish, A. H.; *The Physical Principals of Magnetism*, IEEE Press, New York, **2001**

(40) Dietl, T.; *J.Phys.: Condens. Matter*, **2007**, *19*, 165204/1-165204/15

(41) Kingston, R. H.; *J. Applied Physics*, **1956**, *27*, 101-114

(42) Zhang, L.; Tu, R.; Dai. H. J.; *Nanoletters*, **2006**, *6*, 2785-2789

(43) Woodbury, H. H.; Tyler, W. W.; *Phys. Rev.*, **1955**, *98*, 1534-1535

(44) Wang, D. W.; Chang, Y. L.; Wang, G.; Cao, J.; Farmer, D.B.; Gordon, R. G.; Dai, H. J.; *J. Am. Chem. Soc.*, **2004**, *126*, 11602-11611

(45) Hanrath, T.; Korgel, B. A.; *J. Phys. Chem. B.*, **2005**, *109*, 5518-5524

(46) Ramo, S.; Whinnery, J. R.; Duzer, T. V., *Fields and Waves in Communication Electronics;* Wiley, New York, **1994**

(47) Wang, D.; Wang, Q.; Javey, A.; Tu, R.; Dai, H.; Kim, H.; McIntyre, P. C.; Krishnamohan, T.; Saraswat, K. C.; *Appl. Phys. Lett.*, **2003**, *83*, 2432-2434

(48) Xiang, J.; Lu, W.; Hu, Y.; Wu, Y.; Yan, H.; Lieber, C. M.; *Nature*, **2006**, *441*, 489-493

(49) Wunnicke, O.; *Appl. Phys. Lett*, **2006**, *89*

(50) Zhu, W.; Zhang, Z.; Kaxiras, E., *Phys. Rev. Lett.*, **2008**, *100*, 027205

Table of Contents Figure

Single Crystalline $Ge_{1-x}Mn_x$ Nanowires as Building Blocks for Nanoelectronics